The Astrophysical Journal Letters, 887:L38 (6pp), 2019 December 20 https://doi.org/10.3847/2041-8213/ab5e48

LBT/PEPSI Spectropolarimetry of a Magnetic Morphology Shift in Old Solar-type Stars*

T. S. Metcalfe[1,2], O. Kochukhov[3], I. V. Ilyin[4], K. G. Strassmeier[4], D. Godoy-Rivera[5], and M. H. Pinsonneault[5]
[1] Space Science Institute, 4765 Walnut Street, Suite B, Boulder, CO 80301, USA
[2] Max-Planck-Institut für Sonnensystemforschung, Justus-von-Liebig-Weg 3, D-37077, Göttingen, Germany
[3] Department of Physics and Astronomy, Uppsala University, Box 516, SE-75120 Uppsala, Sweden
[4] Leibniz-Institut für Astrophysik Potsdam (AIP), An der Sternwarte 16, D-14482 Potsdam, Germany
[5] Department of Astronomy, The Ohio State University, 140 West 18th Avenue, Columbus, OH 43210, USA
Received 2019 November 13; revised 2019 December 2; accepted 2019 December 2; published 2019 December 20

Abstract

Solar-type stars are born with relatively rapid rotation and strong magnetic fields. Through a process known as magnetic braking, the rotation slows over time as stellar winds gradually remove angular momentum from the system. The rate of angular momentum loss depends sensitively on the magnetic morphology, with the dipole field exerting the largest torque on the star. Recent observations suggest that the efficiency of magnetic braking may decrease dramatically in stars near the middle of their main-sequence lifetimes. One hypothesis to explain this reduction in efficiency is a shift in magnetic morphology from predominantly larger to smaller spatial scales. We aim to test this hypothesis with spectropolarimetric measurements of two stars that sample chromospheric activity levels on opposite sides of the proposed magnetic transition. As predicted, the more active star (HD 100180) exhibits a significant circular polarization signature due to a nonaxisymmetric large-scale magnetic field, while the less active star (HD 143761) shows no significant signal. We identify analogs of the two stars among a sample of well-characterized *Kepler* targets, and we predict that the asteroseismic age of HD 143761 from future *Transiting Exoplanet Survey Satellite* observations will substantially exceed the age expected from gyrochronology. We conclude that a shift in magnetic morphology likely contributes to the loss of magnetic braking in middle-aged stars, which appears to coincide with the shutdown of their global dynamos.

Unified Astronomy Thesaurus concepts: Solar analogs (1941); Spectropolarimetry (1973); Stellar evolution (1599); Stellar magnetic fields (1610)

1. Background

The coupled evolution of rotation and magnetic activity in solar-type stars has been an active area of research since the pioneering work of Skumanich (1972). The availability of reliable stellar ages has always been a limiting factor, with the earliest studies relying entirely on the Sun and a few young star clusters. The basic picture that emerged was that solar-type stars begin their lives with relatively rapid rotation and strong chromospheric activity, but that both properties gradually decay with the square-root of the age. The Sun was the oldest star with a reliable age beyond 2.5 Gyr (Meibom et al. 2015) until the *Kepler* mission began to yield asteroseismic ages for older field stars (Mathur et al. 2012; Metcalfe et al. 2014; Silva Aguirre et al. 2015). This led to the discovery of unexpectedly rapid rotation in this sample (Angus et al. 2015), which could be understood if magnetic braking becomes much less efficient in solar-type stars beyond the middle of their main-sequence lifetimes (van Saders et al. 2016). A coincident shift in the observed properties and prevalence of chromospheric activity cycles (Metcalfe & van Saders 2017) strongly suggested a magnetic origin for the lower rate of angular momentum loss.

Metcalfe et al. (2016) proposed that the reduced efficiency of angular momentum loss in middle-aged stars could be due to a change in the magnetic field morphology. Charged particles in a stellar wind are tied to the magnetic field lines until they reach the Alfvén radius, which is largest for the dipole component of the field and progressively smaller for higher-order components (Réville et al. 2015). As a consequence of the larger lever-arm, most of the angular momentum loss from magnetized stellar winds can be attributed to the dipole component of the field (See et al. 2019), so a shift in magnetic morphology from larger to smaller spatial scales would reduce the efficiency of magnetic braking. With this in mind, Garraffo et al. (2018) suggested a change in magnetic complexity as a unifying explanation for the persistent fast rotators in young clusters and the anomalously fast rotating old *Kepler* field stars.

There are good reasons why we might have expected a magnetic morphology shift in middle-aged stars. According to van Saders et al. (2016), spin-down stalls at a critical value of the Rossby number, when the rotation period becomes comparable to the convective overturn timescale. In this regime, convection is no longer influenced by substantial Coriolis forces, and the pattern of solar-like differential rotation (i.e., faster at the equator and slower at the poles) either becomes uniform (Featherstone & Hindman 2016), or theoretically might transition to an antisolar pattern (Gastine et al. 2014; Rüdiger et al. 2019). Observationally, two-thirds of the sample of *Kepler* targets with constraints on latitudinal differential rotation from asteroseismic mode-splittings are consistent with uniform rotation, and none are significantly antisolar (Benomar et al. 2018). Metcalfe & Egeland (2019) suggested that the resulting loss of shear might disrupt the production of large-scale magnetic field by the global dynamo, explaining the reduction in angular momentum loss and the

* The LBT is an international collaboration among institutions in the United States, Italy and Germany. LBT Corporation partners are: The University of Arizona on behalf of the Arizona Board of Regents; Istituto Nazionale di Astrofisica, Italy; LBT Beteiligungsgesellschaft, Germany, representing the Max-Planck Society, The Leibniz Institute for Astrophysics Potsdam, and Heidelberg University; The Ohio State University, and The Research Corporation, on behalf of The University of Notre Dame, University of Minnesota and University of Virginia.

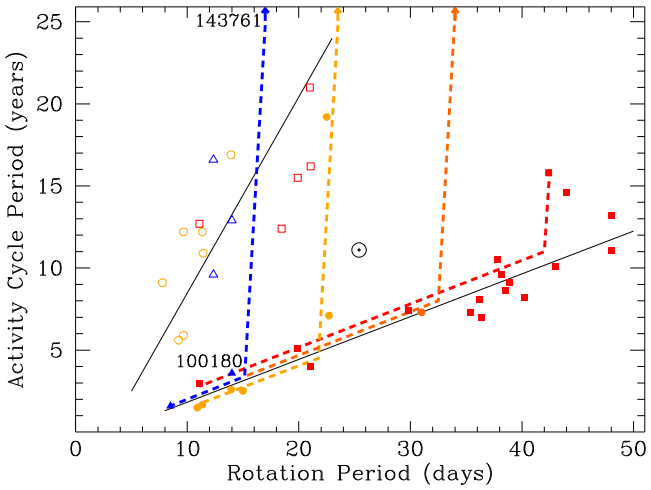

Figure 1. Dependence of activity cycle period on rotation, showing two distinct sequences (solid lines). Points are colored by temperature, indicating F-type (blue triangles), early G-type (yellow circles), late G-type (orange circles), and K-type stars (red squares). Schematic evolutionary tracks are shown as dashed lines (Metcalfe & van Saders 2017), leading to stars with constant activity that appear to have shut down their global dynamos (arrows along the top). Our spectropolarimetric targets are labeled with their HD numbers.

gradual disappearance of activity cycles in stars beyond the middle of their main-sequence lifetimes.

We aim to test for the predicted loss of large-scale magnetic field using spectropolarimetric measurements of two stars on opposite sides of the proposed magnetic transition (see Figure 1). The more active star HD 100180 has a rotation period of 14 days and exhibits dual chromospheric activity cycles with periods of 3.6 and 12.9 yr (Brandenburg et al. 2017). The less active star HD 143761 has a rotation period of 17 days and shows constant chromospheric activity below the solar minimum level over several decades of monitoring at Mount Wilson (Baliunas et al. 1995, 1996). We describe our observations and analysis methods in Section 2. We present the results in Section 3, including an interpretation of the observed Stokes profiles and a comparison of the stellar properties with analogs of the two stars from the *Kepler* mission. We discuss the results in Section 4, including a prediction of what future asteroseismic observations will reveal from the *Transiting Exoplanet Survey Satellite* (*TESS*; Ricker et al. 2014).

2. LBT/PEPSI Observations

We observed HD 100180 and HD 143761 in 2019 May using the Potsdam Echelle Polarimetric and Spectroscopic Instrument (PEPSI; Strassmeier et al. 2015) at the 2 × 8.4 m Large Binocular Telescope (LBT) on Mt. Graham, Arizona, USA. The two polarimetric units, installed at the direct Gregorian focus, were used in circular polarization mode with a quarter-wave polymethylmethacrylate retarder on a rotary stage in front of the polarizing beam-splitting Foster prism unit. The two polarized beams ($I + V$ and $I - V$) are coupled with 200 μm fibers (1.″5 on sky) to render the light into the spectrograph via an image slicer with five slices and a resolving power of $R = 130{,}000$. In polarimetric mode, each spectral order consists of four suborders with the two polarized beams from each of the two telescopes recorded simultaneously. The échelle images are recorded on blue (480.0–544.1 nm) and red (627.8–741.9 nm) channel 10.5 × 10.5 k STA1600LN CCDs with 9 μm pixels and 16 amplifiers.

2.1. Data Reduction

The image processing includes bias subtraction and variance estimation of the source images with subsequent super-master flat-field correction for the CCD spatial noise. Tracing flats are used to define the échelle orders, scattered light is subtracted from every échelle image, and a wavelength solution is obtained from the Th–Ar exposures. The optimal extraction of image slices and the elimination of cosmic-ray spikes is then performed for the target image, with subsequent wavelength calibration and the merging of slices in each order. Normalization to the master flat-field spectrum then removes CCD fringes and the blaze function. Finally, a global 2D fit is made to the continuum of the normalized image, and all spectral orders are rectified into a 1D spectrum for a given cross-disperser.

The continuum of the final polarized spectra was further rectified using the mean spectrum. The weighted average of all spectra was normalized to eliminate any residual effects in the continuum. The ratio of each individual spectrum and the mean is then used to fit a smoothing spline, which constitutes the improved estimate of the true stellar continuum for the individual spectrum.

The polarized spectra were derived with a difference method (Ilyin 2012) to eliminate any first-order residual terms from the quarter-wave retarder due to optical misalignment. Two angles on the retarder were used to obtain polarization states with opposite sense. The difference of the two polarized beams at two angles is combined to obtain Stokes V/I_c, where I_c is the continuum intensity. The intensity spectrum I is the sum of the two polarized beams at two angles. The polarized spectra are treated separately for each polarimeter on the two telescopes, and are averaged with weights to produce the final spectrum (see Strassmeier et al. 2019).

2.2. LSD Profiles

Zeeman polarization signatures are typically not detectable in the individual spectral lines of even the most active late-type stars. A direct detection and quantitative analysis of magnetic field in such cases requires the application of some multiline polarization diagnostic method. Here we used the least-squares deconvolution (LSD; Donati et al. 1997; Kochukhov et al. 2010) technique, which derives high-quality mean intensity and polarization profiles by weighted coaddition of a large number of individual lines. This procedure assumes that all line profiles are self-similar and that overlapping lines add up linearly. The input line data required by the LSD analysis (central wavelengths, effective Landé factors, and line intensities) were retrieved from the VALD database (Ryabchikova et al. 2015) using the stellar parameters from Valenti & Fischer (2005). The final LSD line masks employed for HD 100180 and HD 143761 included 1040–1180 lines deeper than 10% of the continuum. The LSD profiles were calculated with a step of 0.7 km s^{-1}, which corresponds to the largest spacing between consecutive pixels in our PEPSI spectra.

The LSD procedure was applied separately to the four observations of each star (two consecutive integrations with two telescopes) and the resulting profiles were inspected for consistency. One out of the four LSD Stokes V profiles for

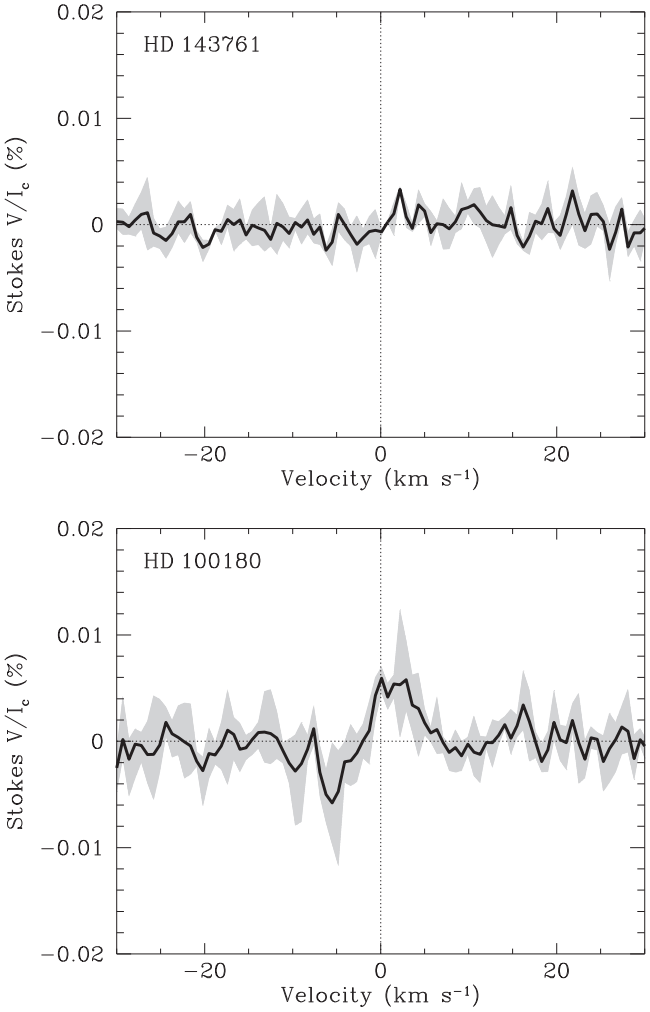

Figure 2. Least-squares deconvolution of the Stokes V profiles for HD 100180 (bottom) and HD 143761 (top). The gray shaded regions show the range of profiles from individual integrations, while the average profile is shown as a dark line. HD 100180 shows the clear signature of a large-scale magnetic field, while HD 143761 shows no significant signal.

HD 143761 exhibited enhanced noise due to issues with the guiding and wavefront sensors on one telescope, and was excluded from further consideration. We have verified that this decision did not change any of the conclusions reported below.

The final average circular polarization LSD profiles of both targets are shown as dark lines in Figure 2, with the full range of the individual integrations shown as gray shaded regions. The formal uncertainty on these mean polarization profiles is (1.1–1.4) $\times 10^{-5}$, representing a polarimetric sensitivity gain of about 50 compared to the original spectra. The LSD Stokes V profile of HD 100180 shows a clear polarization signature with a peak-to-peak amplitude of about 10^{-4}. This observation corresponds to a definite magnetic field detection, characterized by a false alarm probability (FAP) of less than 10^{-10} according to chi-square statistics (Donati et al. 1992, 1997). On the other hand, no evidence of a polarization signal above $\approx 3 \times 10^{-5}$ is seen for HD 143761.

Table 1
Mean Magnetic Field Strengths

	HD 100180	HD 143761
$\langle B_z \rangle$ (G)	-0.42 ± 0.14	-0.27 ± 0.12
$\langle B \rangle_d$ (G)	⋯	$0.48^{+0.76}_{-0.20}$
$\langle B \rangle_q$ (G)	⋯	$1.34^{+2.29}_{-0.45}$
$\langle B \rangle_{ZDI}$ (G)	2.51	⋯

3. Interpretation

3.1. Magnetic Field Properties

We used several methods to characterize the surface magnetic field corresponding to the LSD profiles of HD 100180 and HD 143761. First, we measured the mean longitudinal magnetic field $\langle B_z \rangle$ from the first moment of the Stokes V profile (Kochukhov et al. 2010). This measurement (see Table 1) gives the disk-integrated line-of-sight magnetic field component. For both stars, $\langle B_z \rangle$ is determined with a precision of ∼0.1 G from the PEPSI data. For HD 100180 we obtain $\langle B_z \rangle = -0.42$ G at 3σ significance, confirming the field detection made from the Stokes V profiles. For HD 143761, we obtain a 3σ upper limit of 0.36 G.

Next, we attempted to obtain parameters of the global magnetic field morphologies compatible with our observations. Such analysis is best carried out using the Zeeman Doppler imaging (ZDI) technique (Kochukhov 2016). However, we only have a single-epoch observation for each star rather than a full spectropolarimetric time series. Therefore, we started with a comparison between the observed LSD Stokes V profiles and forward models of the simplest global field configurations: axisymmetric dipole and quadrupole fields. We performed forward polarized radiative transfer calculations using the ZDI code developed by Kochukhov et al. (2014), employing the analytical Unno-Rachkovsky model of the local Stokes parameter profiles. Several parameters of this model were adjusted to match the Stokes I LSD profile assuming $v \sin i = 3.3$ and 1.6 km s^{-1} for HD 100180 and HD 143761 respectively (Valenti & Fischer 2005). Considering the rotation periods reported by Baliunas et al. (1996), and adopting the stellar radii derived by Valenti & Fischer (2005) for consistency, these $v \sin i$ values suggest inclination angles near $i \sim 60°$ and $i \sim 25°$ for HD 100180 and HD 143761 respectively, which we fix for our analysis.

The Stokes V profile of HD 143761 is compatible with an axisymmetric dipole field with a polar field strength of $B_d = -0.7 \pm 1.1$ G, where the error bar corresponds to an FAP $= 10^{-3}$ calculated for the difference between the observed and model Stokes V spectra. Similar analysis assuming an axisymmetric quadrupole field yields $B_q = -2.4 \pm 4.0$ G (see Figure 3, top panel). These upper limits on the polar field strengths can be converted to mean surface field strengths of $0.48^{+0.76}_{-0.20}$ G and $1.34^{+2.29}_{-0.45}$ G for the dipole and quadrupole morphologies respectively.

For HD 100180 an axisymmetric dipole with $B_d = -5$ G roughly matches the observed Stokes V profile amplitude. However, neither dipole nor quadrupole axisymmetric morphologies are able to provide an acceptable fit to the observed shape of the polarization profile. It appears that the surface field geometry of HD 100180 has a dominant nonaxisymmetric component. In an effort to assess its strength, we let the inversion code fit the single Stokes V profile with a

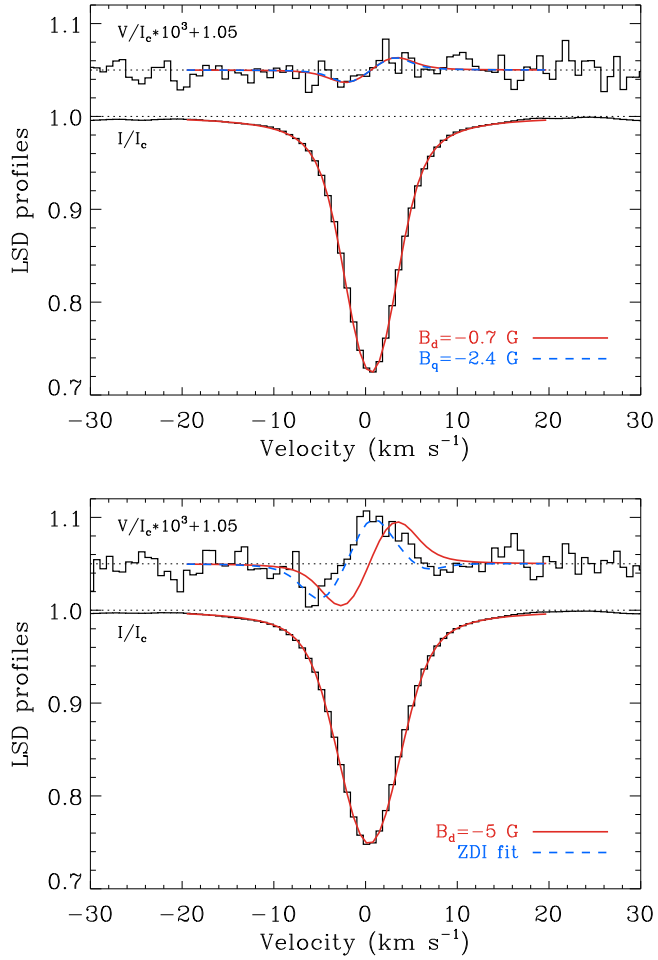

Figure 3. Models of the observed LSD profiles using fixed inclination and various assumptions about the magnetic field morphology for HD 100180 (bottom) and HD 143761 (top). The offset between observations and the dipole model for HD 100180 is due to the nonaxisymmetric components.

general low-order harmonic field parameterization usually employed in the ZDI analyses of solar-type stars (e.g., Petit et al. 2008; Rosén et al. 2016). This calculation yields a nonaxisymmetric field distribution with a peak local field strength of ≈6 G and a mean field strength of 2.51 G (see Figure 3, bottom panel).

3.2. *Analogs from* Kepler

To place the magnetic properties of HD 100180 and HD 143761 in a broader context, we searched for analogs of each star within the sample of asteroseismic targets observed by the *Kepler* mission. Considering stars with detailed asteroseismic modeling from Creevey et al. (2017), we searched for the closest match to both the observed rotation period ($P_{\rm rot}$) and the $B-V$ color. This procedure identified KIC 3427720 as the analog of HD 100180, and KIC 6116048 as the analog of HD 143761.

The properties of our target stars and their *Kepler* analogs are listed in Table 2. For our PEPSI targets, the spectroscopic properties ($T_{\rm eff}$, $\log g$, [Fe/H]) come from the analysis of Valenti & Fischer (2005), while for the *Kepler* analogs we adopt values from Brewer et al. (2016). Rotation periods and chromospheric activity levels ($\log R'_{\rm HK}$) for our targets were determined by Baliunas et al. (1996). For the *Kepler* analogs, rotation periods were determined by Ceillier et al. (2016) and García et al. (2014), while the activity levels were measured by Karoff et al. (2013). Although KIC 3427720 is somewhat more active than HD 100180, and KIC 6116048 is slightly hotter than HD 143761, considering typical uncertainties there is reasonable agreement between the stellar properties for each pair.

Table 2
Spectropolarimetric Targets and *Kepler* Analogs

	HD 100180	KIC 3427720	HD 143761	KIC 6116048
$B-V$	0.57	0.55	0.60	0.59
$T_{\rm eff}$ (K)	5989	6043	5823	6013
$\log g$	4.38	4.35	4.36	4.25
[Fe/H]	−0.02	+0.02	−0.14	−0.14
$P_{\rm rot}$ (days)	14	14 ± 2	17	17 ± 2
$\log R'_{\rm HK}$	−4.92	−4.78	−5.04	−5.02
$t_{\rm gyro}$ (Gyr)	2.1 ± 0.4	2.4 ± 0.4	2.5 ± 0.4	2.7 ± 0.5
$t_{\rm astero}$ (Gyr)	···	2.4 ± 0.2	···	6.1 ± 0.4
$t_{\rm iso}$ (Gyr)	3.6 ± 1.5	3.6 ± 0.7	8.4 ± 1.7	6.5 ± 0.5

References. Valenti & Fischer (2005), Brewer et al. (2016), Baliunas et al. (1996), Ceillier et al. (2016), García et al. (2014), Karoff et al. (2013), Barnes (2007), Creevey et al. (2017).

Using the $P_{\rm rot}$ and $B-V$ color for each star, we calculated an age and uncertainty following the gyrochronology relation of Barnes (2007). For comparison, we tabulate asteroseismic ages from Creevey et al. (2017) for the *Kepler* analogs and isochrone ages from the `isochrones` python package (Morton 2015) for all of the stars, using their spectroscopic properties as input constraints. In order to obtain a robust age estimate for each star, we ran `isochrones` 50 times with each run producing a posterior distribution. We add these into a combined posterior distribution for each star, from which we calculate the age and its uncertainty from the 50th and 16–84th percentiles respectively.

For our more active target HD 100180, there is marginal agreement between the ages deduced from gyrochronology and isochrones. For the *Kepler* analog KIC 3427720, the ages from gyrochronology and asteroseismology are perfectly consistent, while the isochrone age is slightly older. For our less active target HD 143761, there is substantial tension between the ages deduced from gyrochronology and isochrones, with the latter suggesting a much more evolved state. For the *Kepler* analog KIC 6116048, both the asteroseismic and isochrone ages are considerably older than the age suggested by gyrochronology. These results are consistent with the suggestion that rotation and activity decouple near middle-age, making rotation an unreliable age indicator for older stars (Metcalfe & Egeland 2019).

4. Discussion

Stars rotate more slowly over time as they lose angular momentum to magnetized winds, but most of the resulting torque is exerted by the dipole component of the magnetic field (See et al. 2019). Near the middle of a star's main-sequence lifetime, the global dynamo that produces large-scale field apparently begins to shut down (Metcalfe & van Saders 2017). The result is a decoupling of rotation and magnetism near middle-age (Metcalfe & Egeland 2019), a prediction that can be tested observationally with spectropolarimetric measurements. Prior to the transition, more active stars like HD 100180

are expected to exhibit clear signatures of a cycling large-scale magnetic field, and their rotation periods should be reliable age indicators. Beyond the transition, less active stars like HD 143761 are expected to reach a constant activity state without the largest-scale fields that effectively couple rotation and magnetism, so ages from gyrochronology will be inconsistent with those derived from other techniques.

Our spectropolarimetric measurements of HD 100180 reveal the clear signature of a large-scale nonaxisymmetric magnetic field with a mean strength of 2.51 G. By contrast, we do not detect significant polarization in HD 143761, but we can set upper limits on the field strength of a given morphology: 0.48 G for a dipole field, and 1.34 G for a quadrupole field (see Section 3.1). The chromospheric activity level of HD 143761 ($\log R'_{HK} = -5.04$), which is sensitive to magnetic heating on all spatial scales, suggests that overall it is 76% as active as HD 100180 ($\log R'_{HK} = -4.92$). Considering its subsolar metallicity, the corrected activity level of HD 143761 might be slightly lower (Wright 2004; Saar & Testa 2012). This is broadly consistent with the relative strengths of $\langle B_z \rangle$ from our measurements (64%, see Table 1), although the observed correlation between $\log R'_{HK}$ and $\langle B_z \rangle$ for a large sample of stars shows substantial scatter (Marsden et al. 2014). Assuming a fixed morphology, the mean dipole field in HD 143761 is less than 20% as strong as the nonaxisymmetric field in HD 100180, while the quadrupole field would be closer to the observed ratio (53%). The available data are consistent with the predicted disappearance of dipole field in HD 143761, but a complete ZDI analysis of time-resolved spectropolarimetric observations would be required to make this conclusion unambiguous.

The disappearance of large-scale field in stars beyond the middle of their main-sequence lifetimes does not apparently create a discontinuity in the activity–age relation. Measurements of $\log R'_{HK}$ for a sample of spectroscopic solar twins (Lorenzo-Oliveira et al. 2018) and *Kepler* asteroseismic targets (Metcalfe et al. 2016; Booth et al. 2019) both show a smooth evolution across the range of activity levels where the transition to smaller spatial scales is expected to occur ($\log R'_{HK} \approx -4.95$), despite a strong discontinuity in the rotation-age relation (Metcalfe & van Saders 2017). Although this may initially seem surprising, it is understandable considering the weakness of the global dipole field relative to the smaller scale features that mostly cancel in spectropolarimetric measurements. For example, when ZDI maps are synthesized for the Sun-as-a-star, the dipole component of the field has a mean strength $\lesssim$1 G (Vidotto 2016). This can be compared to a mean strength of $\langle B \rangle \sim 170$ G for the unstructured quiet Sun (Danilovic et al. 2010), which dominates the contributions to $\log R'_{HK}$ because the polarity of the field is irrelevant for chromospheric heating. Consequently, disruption of the large-scale organization of the magnetic field as the global dynamo begins to shut down can eliminate the dipole field with no discernible impact on the activity–age relation.

An additional test of our interpretation will be possible when *TESS* obtains asteroseismic observations of HD 143761 in mid-2020. This star is currently scheduled to be observed at a 2 minute cadence for up to 54 days between 2020 April and June, with a high probability of detecting solar-like oscillations (Schofield et al. 2019). Given the large difference between the ages from gyrochronology and isochrones, and considering the asteroseismic age of the *Kepler* analog KIC 6116048, we predict that the asteroseismic age of HD 143761 from *TESS* will be substantially older than expected from its rotation period. By contrast, when *TESS* observes HD 100180 in 2020 February–March, we expect the asteroseismic age to be consistent with gyrochronology.

The authors would like to thank Matthias Rempel, Keivan Stassun, and Regner Trampedach for helpful exchanges. This work benefited from discussions within the international team "The Solar and Stellar Wind Connection: Heating processes and angular momentum loss" at the International Space Science Institute (ISSI). T.S.M. acknowledges support from a Visiting Fellowship at the Max Planck Institute for Solar System Research and from the U.S. National Science Foundation under grant AST-1812634. O.K. acknowledges support by the Knut and Alice Wallenberg Foundation (project grant "The New Milky Way"), the Swedish Research Council (projects 621-2014-5720, 2019-03548), and the Swedish National Space Board (projects 185/14, 137/17). K.G.S. thanks the LBTO for the flexible PEPSI scheduling, and the German Federal Ministry BMBF and the Brandenburg State Ministry MWFK for funding PEPSI. D.G.R. and M.H.P. acknowledge support from NASA ADP grant 80NSSC19K0597.

ORCID iDs

T. S. Metcalfe https://orcid.org/0000-0003-4034-0416
O. Kochukhov https://orcid.org/0000-0003-3061-4591
K. G. Strassmeier https://orcid.org/0000-0002-6192-6494
M. H. Pinsonneault https://orcid.org/0000-0002-7549-7766

References

Angus, R., Aigrain, S., Foreman-Mackey, D., et al. 2015, MNRAS, 450, 1787
Baliunas, S., Sokoloff, D., & Soon, W. 1996, ApJL, 457, L99
Baliunas, S. L., Donahue, R. A., Soon, W. H., et al. 1995, ApJ, 438, 269
Barnes, S. A. 2007, ApJ, 669, 1167
Benomar, O., Bazot, M., Nielsen, M. B., et al. 2018, Sci, 361, 1231
Booth, R. S., Poppenhaeger, K., Watson, C. A., et al. 2019, MNRAS, in press (arXiv:1910.12557)
Brandenburg, A., Mathur, S., & Metcalfe, T. S. 2017, ApJ, 845, 79
Brewer, J. M., Fischer, D. A., Valenti, J. A., et al. 2016, ApJS, 225, 32
Ceillier, T., van Saders, J., García, R. A., et al. 2016, MNRAS, 456, 119
Creevey, O. L., Metcalfe, T. S., Schultheis, M., et al. 2017, A&A, 601, A67
Danilovic, S., Schüssler, M., & Solanki, S. K. 2010, A&A, 513, A1
Donati, J.-F., Semel, M., Carter, B. D., et al. 1997, MNRAS, 291, 658
Donati, J.-F., Semel, M., & Rees, D. E. 1992, A&A, 265, 669
Featherstone, N. A., & Hindman, B. W. 2016, ApJL, 830, L15
García, R. A., Ceillier, T., Salabert, D., et al. 2014, A&A, 572, A34
Garraffo, C., Drake, J. J., Dotter, A., et al. 2018, ApJ, 862, 90
Gastine, T., Yadav, R. K., Morin, J., et al. 2014, MNRAS, 438, L76
Ilyin, I. 2012, AN, 333, 213
Karoff, C., Metcalfe, T. S., Chaplin, W. J., et al. 2013, MNRAS, 433, 3227
Kochukhov, O. 2016, Lecture Notes in Physics (Berlin: Springer), 177
Kochukhov, O., Lüftinger, T., Neiner, C., et al. 2014, A&A, 565, A83
Kochukhov, O., Makaganiuk, V., & Piskunov, N. 2010, A&A, 524, A5
Lorenzo-Oliveira, D., Freitas, F. C., Meléndez, J., et al. 2018, A&A, 619, A73
Marsden, S. C., Petit, P., Jeffers, S. V., et al. 2014, MNRAS, 444, 3517
Mathur, S., Metcalfe, T. S., Woitaszek, M., et al. 2012, ApJ, 749, 152
Meibom, S., Barnes, S. A., Platais, I., et al. 2015, Natur, 517, 589
Metcalfe, T. S., Creevey, O. L., Doğan, G., et al. 2014, ApJS, 214, 27
Metcalfe, T. S., & Egeland, R. 2019, ApJ, 871, 39
Metcalfe, T. S., Egeland, R., & van Saders, J. 2016, ApJL, 826, L2
Metcalfe, T. S., & van Saders, J. 2017, SoPh, 292, 126
Morton, T. D. 2015, isochrones: Stellar model grid package, Astrophysics Source Code Library, ascl:1503.010
Petit, P., Dintrans, B., Solanki, S. K., et al. 2008, MNRAS, 388, 80
Réville, V., Brun, A. S., Matt, S. P., et al. 2015, ApJ, 798, 116

Ricker, G. R., Winn, J. N., Vanderspek, R., et al. 2014, Proc. SPIE, 9143, 914320
Rosén, L., Kochukhov, O., Hackman, T., et al. 2016, A&A, 593, A35
Rüdiger, G., Küker, M., Käpylä, P. J., et al. 2019, A&A, 630, A109
Ryabchikova, T., Piskunov, N., Kurucz, R. L., et al. 2015, PhyS, 90, 054005
Saar, S. H., & Testa, P. 2012, in IAU Symp. 286, Comparative Magnetic Minima: Characterizing Quiet Times in the Sun and Stars, ed. C. H. Mandrini & D. F. Webb (Cambridge: Cambridge Univ. Press), 335
Schofield, M., Chaplin, W. J., Huber, D., et al. 2019, ApJS, 241, 12
See, V., Matt, S. P., Finley, A. J., et al. 2019, ApJ, 886, 120
Silva Aguirre, V., Davies, G. R., Basu, S., et al. 2015, MNRAS, 452, 2127
Skumanich, A. 1972, ApJ, 171, 565
Strassmeier, K. G., Carroll, T. A., & Ilyin, I. V. 2019, A&A, 625, A27
Strassmeier, K. G., Ilyin, I., Järvinen, A., et al. 2015, AN, 336, 324
Valenti, J. A., & Fischer, D. A. 2005, ApJS, 159, 141
van Saders, J. L., Ceillier, T., Metcalfe, T. S., et al. 2016, Natur, 529, 181
Vidotto, A. A. 2016, MNRAS, 459, 1533
Wright, J. T. 2004, AJ, 128, 1273